AFOSR·TR· 87-0181

AD-A177 405

Thermodynamics of High Temperature Materials

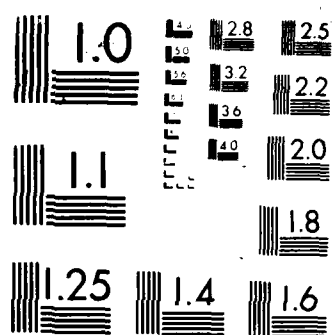Annual Report for the Period

1 October 1985 - 30 September 1986

AIR FORCE OFFICE OF SCIENTIFIC RESEARCH

AFOSR-ISSA-86-0032

MAR 3 1987

A

REPORT DOCUMENTATION PAGE

1a. REPORT SECURITY CLASSIFICATION UNCLASSIFIED		1b. RESTRICTIVE MARKINGS AI77405			
2a. SECURITY CLASSIFICATION AUTHORITY		3. DISTRIBUTION/AVAILABILITY OF REPORT			
2b. DECLASSIFICATION/DOWNGRADING SCHEDULE		Approved for public release; distribution unlimited.			
4. PERFORMING ORGANIZATION REPORT NUMBER(S)		5. MONITORING ORGANIZATION REPORT NUMBER(S) AFOSR-TR- 87-0181			
6a. NAME OF PERFORMING ORGANIZATION National Bureau of Standards	6b. OFFICE SYMBOL (If applicable)	7a. NAME OF MONITORING ORGANIZATION AFOSR			
6c. ADDRESS (City, State and ZIP Code) Thermonynamics Division Gaithersburg, MD 20899		7b. ADDRESS (City, State and ZIP Code) BDa 410 Bolling AFB DC 20332			
8a. NAME OF FUNDING/SPONSORING ORGANIZATION AFOSR	8b. OFFICE SYMBOL (If applicable) NE	9. PROCUREMENT INSTRUMENT IDENTIFICATION NUMBER AFOSR-ISSA- 86-0035			
8c. ADDRESS (City, State and ZIP Code) Same as 7b		10. SOURCE OF FUNDING NOS.			
11. TITLE (Include Security Classification) Thermodynamics of High Temperature Materials		PROGRAM ELEMENT NO. 61102F	PROJECT NO. 2306/	TASK NO. A2	WORK UNIT NO.

12. PERSONAL AUTHOR(S)
Dr Stanley Abramowitz

13a. TYPE OF REPORT Annual	13b. TIME COVERED FROM 1-10-85 TO 30-9-86	14. DATE OF REPORT (Yr., Mo., Day)	15. PAGE COUNT

16. SUPPLEMENTARY NOTATION

17.	COSATI CODES		18. SUBJECT TERMS
FIELD	GROUP	SUB. GR.	

19. ABSTRACT (Continue on reverse if necessary)

The research described encompasses five tasks each of which treats, from either an experimental or theoretical base, the measurement or interpretation of the high-temperature thermophysical behavior of model systems which show potential applications to the environmental resistant materials and the spacecraft survivability programs. Measurements have been completed, in a specially designed apparatus using state of the art pyrometery, on the triple point of graphite by a pulse heating method. Calculational algorithms based have been expanded to calculate direct radiative interactions among many coupled channels and provide the continuum-continuum matrix elements needed to describe photodissociation phenomena. A combined theoretical and experimental program is being pursued to increase the understanding of the relationship of structure and reactivity of graphitic species. The rates and mechanism of ionic polymerization in highly unsaturated organic compounds, structures and thermochemistry of relevant ions, photodissociation of the polymeric ions, and the repair which generate polymeric ions after photodissociation have been studied. Development of apparatus and techniques to study the molecular basis for laser induced vaporization of refractory materials such as graphite continued.

20. DISTRIBUTION/AVAILABILITY OF ABSTRACT UNCLASSIFIED/UNLIMITED ☐ SAME AS RPT ☐ DTIC USERS ☐	21. ABSTRACT SECURITY CLASSIFICATION UUUU	
22a. NAME OF RESPONSIBLE INDIVIDUAL Joseph Hager Major USAF	22b. TELEPHONE NUMBER (Include Area Code) 767-4933	22c. OFFICE SYMBOL NE

DD FORM 1473, 83 APR   EDITION OF 1 JAN 73 IS OBSOLETE.

TABLE OF CONTENTS

ABSTRACT

The research described encompasses five tasks each of which treats, from either an experimental or theoretical base, the measurement or interpretation of the high-temperature thermophysical behavior of model systems which show potential applications to the environmental resistant materials and the spacecraft survivability programs. While there is significant overlap between these tasks, the first chapter is addressed to the environmental resistant materials programs, while the later four chapters are addressed to the spacecraft survivability program.

Measurements have been completed, in a specially designed apparatus using state of the art pyrometery, on the triple point of graphite by a pulse heating method. The surface radiance temperature of melting graphite at a wavelength of 655nm is 4330 K, while the triple point is estimated to be 4530 K with an estimated uncertainty of 150 K.

Calculational algorithms based have been expanded to calculate direct radiative interactions among many coupled channels and provide the continuum-continuum matrix elements needed in lineshape theory as well as the bound-continuum matrix elements needed to describe photodissociation phenomena. Calculations have been made to study pressure broadening of atomic lines in both weak and strong laser fields. Power broadening and saturation of continuum transitions in intense multiphoton fields have also been explored.

A combined theoretical and experimental program is being pursued to increase the understanding of the relationship of structure and reactivity of graphitic species. This program focusses on the fundamental chemical properties of very large polyaromatic species. Theoretical methods have been developed that can reliably predict structure and reactivity of large

graphitic structures. This theory, a modified Huckel approach, accurately predicts enthalpies of formation of pi-radicals. A high temperature, low pressure flow reactor has been built. This apparatus, which has a capability to 3000 K, will be used to test some of the results of the theoretical program.

The rates and mechanism of ionic polymerization in highly unsaturated organic compounds, structures and thermochemistry of relevant ions, photodissociation of the polymeric ions, and the repair mechanisms which generate polymeric ions after photodissociation have been studied. The work focussed on the structure and reactivity of the phenylium ion, which is ubiquitous in irradiated aromatic systems. Both the formation of this ion and its reaction have been studied. Ionic condensation mechanisms, which occur without activation barriers have also been studied.

Development of apparatus and techniques to study the molecular basis for laser induced vaporization of refractory materials such as graphite continued. The effects of laser energy, optical and sample geometry and sample morphology on the distribution of the vapor phase species of carbon ablated from a selection of graphites has been examined. Improvements have been made in the experimental apparatus and the modelling of the results.

DETERMINATION OF THE TRIPLE-POINT TEMPERATURE OF GRAPHITE FROM MEASUREMENTS BY A PULSE-HEATING TECHNIQUE

A. Cezairliyan and A. P. Miiller

ABSTRACT

Measurements of spectral radiance of graphite in the vicinity of its triple point have been performed by a rapid pulse-heating technique. The method is based on: (a) resistively heating the specimen in a pressurized gas environment (~200 atm) from room temperature to its melting point in less than 20 ms by passing an electrical current pulse through it; and (b) simultaneously measuring the radiance temperature of the specimen surface at 655 nm every 120 us by means of a high-speed pyrometer. The results for two different grades of POCO graphite (DFP-1 and AXM-5Q1) are in good agreement and yield a value of 4330 ± 50 K for the spectral radiance temperature (at 655 nm) at the triple point. On the basis of the present value and literature data for normal spectral emittance, the true triple-point temperature of graphite is estimated to be 4530 ± 150 K.

1. INTRODUCTION

During the past decade or so, there have been numerous studies of the solid-liquid-vapor triple-point of graphite reported in the literature (see reviews in Refs.[1,2]). Most measurements of triple-point pressure have yielded values in the range of about 100-110 atm. However, the reported measurements of triple-point temperature are in considerable disagreement, yielding values which span the range of approximately 4000 to 5000 K. The major problem in such measurements arises from the high vapor pressure of graphite at elevated temperatures: as the triple-point is approached, a plume of cooler carbon vapor or soot forms near the specimen surface, thereby severely limiting the accuracy of optical pyrometry.

A feasibilty study [3] in our laboratory has shown that effects of specimen evaporation on pyrometric temperature measurements can be suppressed or at least minimized under certain conditions, namely: (1) the pressurized inert gas environment of the specimen must contain a small amount of oxygen to combine with the opaque carbon vapor, forming optically transparent gases CO and CO_2; (2) the specimen heating rate must be about $10^5 K \cdot s^{-1}$ or higher to minimize the effect of convective turbulence on the sighting path of the pyrometer.

As a result of this study, a high-speed six-wavelength pyrometer was designed and constructed [4] to provide a means of estimating true temperature of a rapidly-heated specimen from accurate measurements of surface radiance. Measurements to determine the triple-point temperature of graphite were then initiated [5]. Unfortunately, accurate results for temperature were precluded by a long-term drift in the response of the new pyrometer discovered during the course of successive calibration experiments. The source of instability was subsequently determined to be the interference filters which have now been replaced.

The present report briefly describes (a) recent measurements on two different grades of POCO graphite at temperatures in the vicinity of the triple point, (b) results for the radiance temperature (at 655 nm) of graphite at its triple point from which an estimate of the true triple-point temperature is made. An alternative method of determining true temperature is also briefly discussed.

2

2. MEASUREMENTS AND RESULTS

Details regarding the construction and operation of the measurement system, which includes an electric power-pulsing circuit, a high-pressure experiment chamber, the multi-wavelength pyrometer, and a digital storage oscilloscope, are given in the previous report [5]. A significant improvement in time resolution (a factor of six) was achieved in the present work by replacing the digital scope with a new data acquisition system capable of digitizing the pyrometer signals with 13-bit resolution at rates of up to 100 kHz.

The first step in the two-stage calibration of the six-wavelength pyrometer has been completed. It involves calibrating the 655 nm "channel" in a steady-state experiment with a tungsten-filament lamp which, in turn, had been calibrated against the NBS Photoelectric Pyrometer operating at the same effective wavelength. The second step consists of transferring the calibration to the other five channels (centered at 500, 600, 700, 800, and 900 nm) by means of a steady-state blackbody furnace. A graphite furnace, which has been recently installed for this purpose, is currently being tested to determine its blackbody quality.

Specimens were fabricated in the form of rectangular strips from graphite material which was supplied by the manufacturer in the form of thin (0.5 mm) sheets and designated as either POCO DFP-1 or POCO AXM-5Q1. The nominal dimensions of each strip was

3

25 mm long by 3 mm wide. The center portion of each strip was "necked-down" in order to define a small "effective" specimen with nominal dimensions of 2mm long by 1 mm wide. This procedure reduced the effective surface area of the specimen and hence, the amount of carbon vapor released since melting was limited to the effective portion only.

Prior to each pulse experiment, a strip specimen was mounted vertically inside the experiment chamber which was then filled with the desired amount of oxygen (partial pressures in the range of 150 to 600 psig) and finally pressurized with argon to approximately 3000 psig (~200 atm). Upon equilibration of the gas mixture, the circular viewing target (diameter = 0.5 mm) of the pyrometer was focussed on the surface of the "effective" specimen. The specimen was then rapidly heated from room temperature to its melting temperature in less than 20 ms by passing an electrical current pulse through it. The heating rate varied with experiment in the range 2×10^5 to 5×10^5 $K \cdot s^{-1}$.

The variation of surface radiance temperature (at 655 nm) with elapsed time during a typical pulse-heating experiment is presented in Fig.1. The plateau in the temperature-time function is a characteristic of solid to liquid transformations; the glassy appearance of the remaining portion of effective specimen provided further evidence that melting had occurred. In all cases, the plateau radiance temperature, which is indicated by the horizontal line in Fig.1, was taken as the maximum temperature along the initial flat portion of the plateau.

The results for plateau radiance temperature determined from rapid melting experiments on two different grades (DFP-1 and AXM-5Q1) of POCO graphite are summarized in Fig. 2. As may be seen, the plateau temperature decreases linearly with oxygen content in the pressurizing gas enviroment. The effect appears to arise from the reaction of carbon in the specimen surface with excess oxygen in the immediate vicinity of the specimen; the reaction (combustion) produces additional visible radiation which is detected by the pyrometer. This suggests that the "correct" radiance temperature at melting may be determined by extrapolating the measured values to zero oxygen content.

The values of plateau radiance temperature were fitted by a linear function of oxygen partial pressure by means of the least-squares method; the function is represented by the solid straight line in Fig. 2. Upon extrapolation to zero oxygen content, the function yielded a value of 4330 K for the radiance temperature (at 655 nm) of graphite at its triple point.

The major sources of error in the temperature data arise from (1) calibration and operation of the pyrometer, and (2) physical and chemical conditions of each specimen.

A detailed analysis of sources and magnitudes of the errors in temperature measurements with a similar high-speed pyrometer is given in a earlier publication [6]. Allowing for differences between present operational conditions and those in the earlier study, we estimate the maximum error attributable to pyrometry to be about 25 K.

The errors arising from specimen conditions are considerably more difficult to assess. A measure of variability in specimen conditions is given by the maximum range of plateau radiance temperatures observed for a given oxygen content (see Fig. 2), which is about 20 K. There is also an additional uncertainty associated with assigning the present value of 4330 K to the triple point since our measurements were performed at ~200 atm rather than at the triple-point pressure of ~100 atm. However, this error appears to be small, less than 2 K, on the basis of the T-P phase for carbon determined by Bundy [7].

Thus, the total uncertainty (errors due to pyrometry and specimen conditions) in the reported radiance melting temperature is estimated to be not more than ± 50 K. It may be concluded that the radiance temperature (at 655 nm) of graphite at its triple point is 4330 ± 50 K.

True temperature may be determined from measured spectral radiance temperature by means of Planck's law if the normal spectral emittance is known at the given wavelength. A data compilation on thermal radiative properties by Touloukian and DeWitt [8] shows that, for different surface conditions, the normal spectral emittance (between 650 and 665 nm) of graphite is in the range 0.8 to 0.9 at 1500 K and that, this property is a slowly varying function of temperature. By extrapolating the trend in values between 1100 and 3300 K to temperatures approaching the triple point, we estimate the normal spectral emittance (at 655nm) of graphite at its triple point to be 0.8 ± 0.1. On

the basis of the extrapolated value for emittance and the present value for radiance temperature, the true triple-point temperature of graphite is estimated to be 4530 ± 150 K.

3. CONCLUDING REMARKS

Additional pulse-heating experiments on graphite are planned when the multi-wavelength pyrometer is fully calibrated; these must await final tests on the steady-state blackbody furnace which will be used to transfer the calibration of the 655 nm "channel" to the other five wavebands, centered at effective wavelengths between 500 and 900 nm. Spectral radiance data in six wavebands should yield a more accurate estimate for normal spectral emittance of graphite at its triple point and thereby, a better estimate for the true triple-point temperature.

An alternative method of measuring the true triple-point temperature is also being studied. This involves similar rapid melting experiments but with graphite specimens which are fabricated in the form of thin-walled tubes having nominal dimensions: 25 mm length, 3 mm outside diameter, 0.5 mm wall thickness. Each tube is mounted horizontally inside the high-pressure chamber and the pyrometer is sighted axially into one of the open ends, thereby approximating blackbody conditions. As yet, these experiments have not yielded meaningful temperature data due to problems associated with carbon vapor condensation at the clamped (cold) ends of the tube. The results suggest that significantly higher heating rates may be required.

7

4. REFERENCES

1. F. P. Bundy, J. Geophysical Research 85, 6930 (1980).

2. M. A. Sheindlin, High Temperature 19, 467 (1981).

3. A. Cezairliyan, A. P. Miiller and J. L. McClure, Report AFOSR-ISSA-83-00038, 1983, p.1.

4. G. M. Foley, to be published.

5. A. Cezairliyan, A. P. Miiller and J. L. McClure, Report AFOSR-ISSA-85-00029, 1985, p.1.

6. A. Cezairliyan, M. S. Morse, H. A. Berman and C. W. Beckett, J. Res. Natl. Bur. Stand.(U.S.) 74A, 65 (1970).

7. F. P. Bundy, J. Chem. Phys. 38, 618 (1963).

8. Y. S. Touloukian and D. P. DeWitt, Thermophysical Properties of Matter, Vol.8, Thermal Radiative Properties of Nonmetallic Solids (IFI/Plenum, New York, 1970).
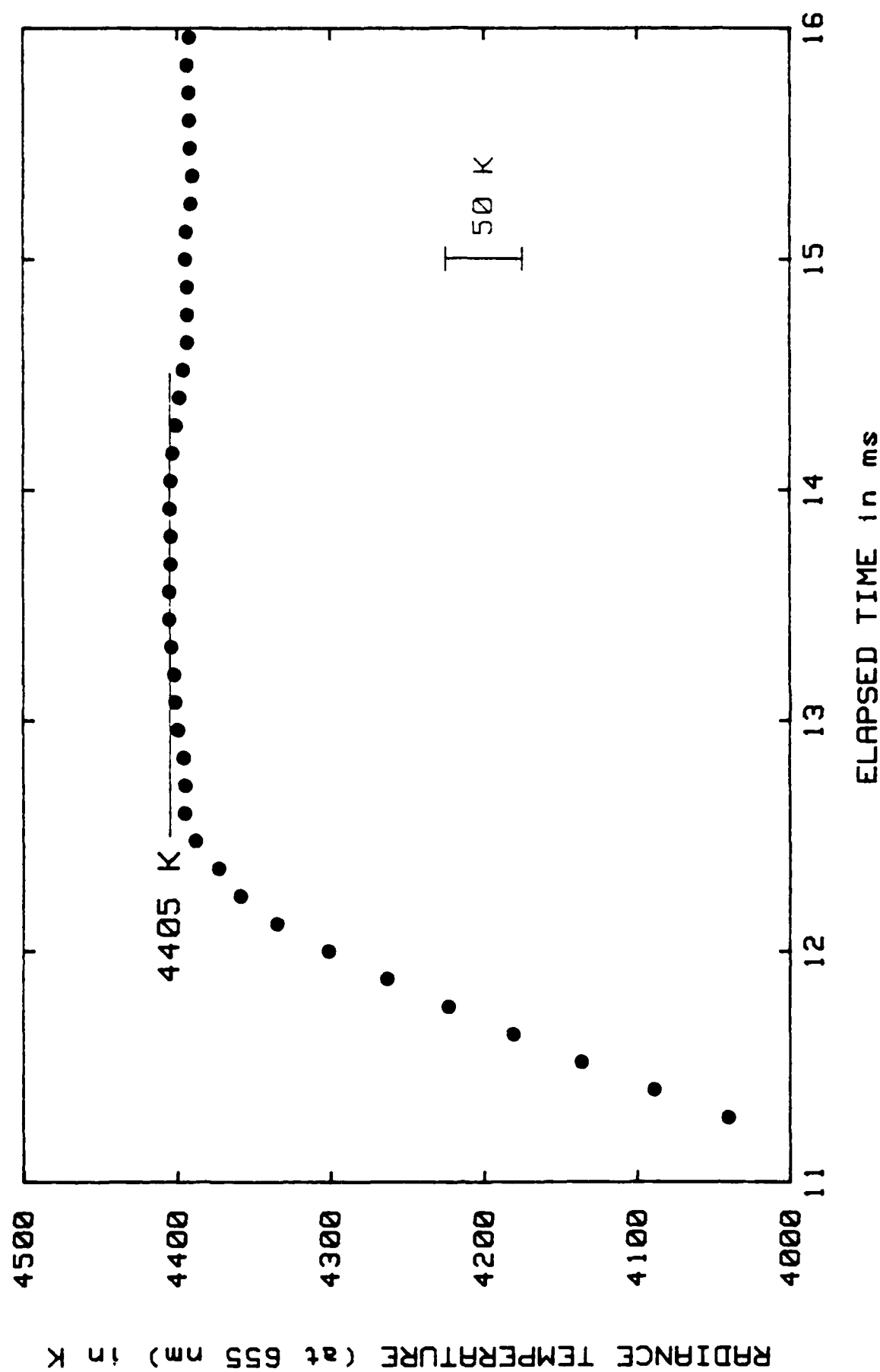
Fig. 1. Variation of radiance temperature (at 655 nm) of the specimen surface as a function of time during a typical experiment in which the specimen was pulse-heated from room temperature to its melting point in a pressurized gas environment (80% argon, 20% oxygen) at 3000 psig.
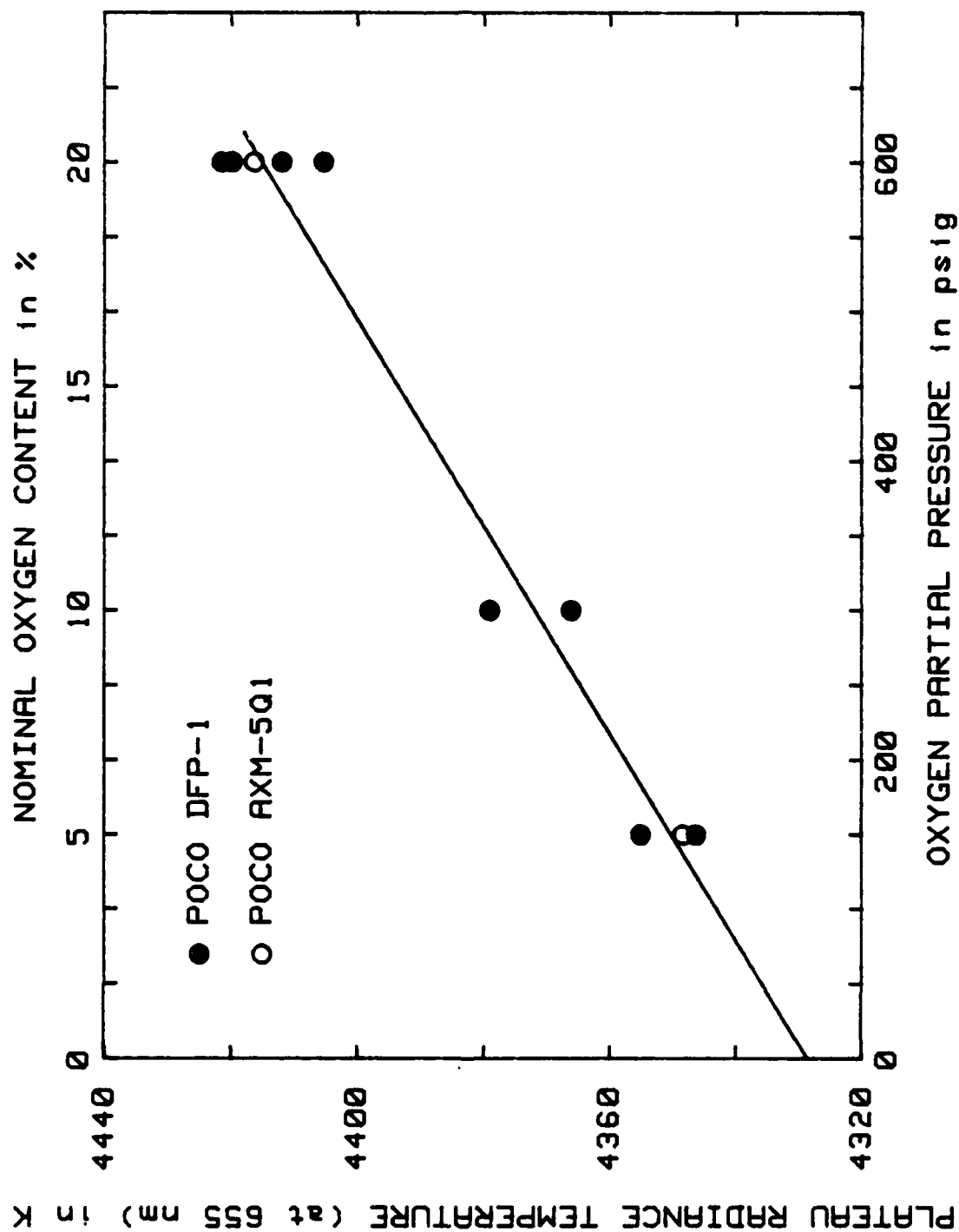
Fig. 2. Radiance temperature (at 655 nm) at the melting plateau of DFP-1 and AXM-5Q1 POCO graphite as a function of oxygen content in the argon gas environment pressurized at 3000 psig.

Broad-Band Spectroscopy of Small Molecules in
Intense Laser Fields

Principal Investigators: P.S. Julienne and F. H. Mies

Introduction

The general goal of this research is to provide calculations of
radiative cross-sections, fragment state distributions, and intense laser
saturation effects for broad-band, wavelength insensitive continuum
spectral features of small gaseous molecules of possible interest in
spacecraft survivability. Specifically our goal is to understand the
interaction of intense laser radiation with gaseous material either burned
off or deliberately released from a target. In addition to providing data
of possible use in designing heat shields and reflective coatings,
knowledge of the resultant fluorescence of ablated surface material during
and following laser illumination of a target might serve as a useful tool
in discrimination between heavy targets and lightweight decoys.

Theoretical input into this program is provided by extensive sets of
computer codes available to the quantum chemistry group. State of the art
calculations of any necessary molecular potentials, couplings and radiative
transition dipoles can be obtained. Scattering codes provide rigorous
non-pertubative radiative scattering matrix elements needed to evaluation
attenuation coefficients for intense, saturating laser radiation
propagating through gaseous vapors. Of necessity, the program also involves
extensive analysis of many new theoretical features introduced by very
intense laser fields.

Summary of Accomplishments in FY 1986.

Our original intention for this year was to concentrate on the
development and expansion of our photodissociation codes since we
envisioned this as the principal broad-band absorption mechanism that might
contribute to passive spacecraft shielding. However, after attending the
1985 AFOSR conference on Laser-Material Interactions in Albuquerque, we

became convinced that, because of the high pressures and temperatures associated with laser ablated vapors, we should place greater emphasis on the study of the lineshapes of pressured broadened atomic and molecular transitions in intense laser fields as a possible mechanism for absorbing incoming laser radiation.

Our scattering programs have been expanded to allow for direct radiative interactions among many coupled channels, and now provide the continuum-continuum scattering matrix elements needed in lineshape theory, as well as the bound-continuum matrix elements required to describe photodissociation. Several calculations have been performed to study the pressure broadening of atomic lineshapes in both weak and strong laser fields. In particular we have gained extensive experience in calculating very accurate nonadiabatic effects in the conventional weak-field limit, and have performed preliminary calculations which exhibit the power broadening and the saturation of continuum transitions in intense, multiphoton fields. Manifestations of a.c. stark shifts and the laser-induced Mollow lineshape associated with the dressing of fragments by the radiation field are extracted from the numerical results. This suggests that normal perturbation theory as applied to radiative interactions must be carefully scrutinized when applied to laser attenuation mechanisms.

Scattering in the Presence of Radiation

The general goal of this research is to provide calculations of radiative cross-sections and fragment state distributions associated with the collisional broadening and photodissociation of small molecules. This year we have developed extensive experience in calculating various nonadiabatic effects in the conventional weak-field limit, and have expanded our codes to treat the saturation of continuum transitions in intense, multiphoton fields.

1. Non-adiabatic Theory of Atomic Broadening in Weak Fields.

(a) Redistribution Calculations for $Sr(^1P \leftarrow {}^1S)$ + Ar. We completed our close-coupled calculations of polarized light redistribution in the Sr + Ar system. The calculations predict the polarization ratios of $Sr(^1P)$ fluorescence following line wing excitation by either linear or circular

polarized light. Ab initio calculations were used to obtain the ground and excited SrAr molecular potentials, which were adjusted modestly to give improved agreement with experiment. The radiative scattering theory gives a unified description of the absorption coefficient and subsequent fluorescence from the small detuning impact limit region to the far wings. The cross sections for depolarizing collisions of $Sr(^1P) + Ar$ were also calculated. The calculated absorption coefficient, impact broadening rate, linear and circular polarization ratios, and depolarization rate coefficients are for the most part in good agreement with a diverse set of experimental data.

(b) Redistribution Calculations for Na + Rare Gas. We have used our close-coupled codes to calculate final state branching ratios for fine structure states and alignment/orientation for $Na(^2P\leftarrow^2S)$ + He,Ne,Ar systems, and have obtained good agreement with experimental measurements. In analysing the exact close-coupled data we uncovered a useful spin-uncoupling approximation of the collision dynamics and its dependence on collision velocity.

(c) Lorentzian Pressure-Broadened widths for Na. We have calculated the Lorentzian pressure-broadened widths for both the D1 and D2 lines of Na broadened by collisions with He, Ne, and Ar. In addition we have performed the first calculation of the so-called asymmetry parameter which has been widely observed in the impact regions of atomic lineshapes. The absorption profile within the impact limit for one of the isolated ^2P_j fine structure lines may be written as

$$I(\Delta_j) = \frac{\gamma_j(\Delta_j)/\pi}{(\Delta_j - \delta_j)^2 + \gamma_j^2(0)}$$

where Δ_j and δ_j are the respective detunings and shift of the line. The detuning-dependent quantity $\gamma_j(\Delta_j)$ may be shown to have a finite limit as $\Delta_j \rightarrow 0$ and exactly equals the usual impact limit broadening coefficient, including the effects of both elastic and inelastic collisions. The dependence on detuning gives rise to the Lorentzian dispersion asymmetry which has been observed for Na + rare gas systems. We have calculated the radiative scattering cross section for detunings near the D1 and D2 lines

for Na broadened by He, Ne and Ar. The widths and asymmetry parameters are qualitatively in agreement with measured values. Deficiencies in the existing molecular potentials limit the expected accuracy of the scattering calculations.

2. Nonadiabatic Theory of Redistribution in Strong Fields

(a) Collisional Redistribution of Resonant Radiation. Close-coupling codes developed for scattering in the presence of radiation fields have been used to calculate the pressure broadening and collisional depolarization of the Sr resonance transition in strong saturating fields

$$Sr(^1S) + Ar + \hbar\omega_L \rightarrow Sr*(^1P) + Ar \rightarrow Sr(^1S) + Ar + \hbar\omega$$
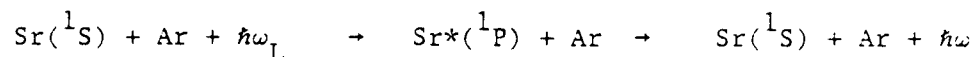
As we increase the Rabi frequency Ω_L and decrease the detuning Δ_L of the incident laser three observable properties associated with optical collision processes are obtained from such calculations:

(i) Impact Limit Lineshape. As $\Delta_L \rightarrow 0$ we can demonstrate that proper pressure broadened half widths, which include both elastic and inelastic collisional effects, can be rigorously extracted from close-coupled radiative scattering matrix element. The first manifestations of a.c. stark shifts associated with the dressing of fragments by the radiation field are extracted from the numerical results, and confirms the anticipated power broadening of the Lorenztian absorption profile. This suggests that normal perturbation theory as applied to radiative interactions must be carefully scrutinized.

(ii) Inelastic transitions involving dressed atomic states. As Ω_L increases and eventually exceeds Δ_L the asymptotic Sr atomic states become dressed. Our fully quantal inelastic cross-sections can be used to calculate population dedistribution rates in the presence of intense fields.

(iii) Collisional redistribution spectra in saturating fields. In strong fields we obtain the redistribution spectra for $\hbar\omega_R$ in the impact limit and find the typical three-peaked Mollow lineshape due to fluorescence between dressed atomic states. Both the half-width and the polarization of the emission peaks are calculated.

(b) Analysis of Multiphoton Lineshape Theory in Intense Fields. One of the most critical ingredients in understanding the interaction of

14

colliding atoms and molecules with intense, multimoded laser fields is the calculation of collisional lineshapes and the associated relaxation rates for the optically pumped energy levels. In particular these are needed to define the redistribution spectra which might serve as a diagnostic of the laser-induced vapors. Two complimentary theoretical approaches are used to describe these phenomena. The first is represented by our "optical collision" approach here at NBS where we calculate the radiative scattering matrix elements for atom-atom scattering in the presence of intense monochromatic laser fields. The calculations incorporate many subtle and sophisticated non-adiabatic and inelastic effects which are often neglected in conventional lineshape theory. However, these data that we generate must then be incorporated into very subtle and complicated theoretical expressions for the density matrix of the interacting molecules in the field of the pumping laser fields. Only then do our calculations yield the proper description of the redistributed radiation.

The second theoretical approach is exemplied by the tetradic formalism developed by Prof. Ben-Reuven at Tel Aviv University using a Liouvillian analysis of the molecular density matrix in the presence of collisions. Fortunately, the formal ingredients of this sophisticated theory are the very scattering matrix elements that are generated by our optical collision approach.

We have begun a collaboration with Prof. Ben-Reuven to explore the relationship between the tetradic description of redistribution and the close-coupled theory of scattering in strong multiphoton fields. So far we have successed in showing the explicit relationships required to analyze resonance fluorescence and resonant Raman lineshapes.

Atomic and Molecular Scattering Theory

1. Half-Collision Amplitudes - Analysis of Exact Close-Coupled Codes. We have previously used a multichannel quantum defect analysis (MCQDA) of exact close-coupled radiative matrix elements to show that these can often be factored as follows

$$S_{fi}^{rad} = N_{ff'}^{-} S_{f'i'}^{BO} N_{i'i}^{+}$$

where the 'incoming' half-collision matrix $N_{i',i}^{+}$ tracks the non-adiabatic scattering of the incident collision complex, and $N_{f,f'}^{-}$ summarizes the inelastic behavior of the 'outgoing', radiatively excited collision complex. We have speculated on the unitarity of these matrices which would justify the persistent used of the pure adiabatic Born-Oppenheimer matrix element $S_{f'i'}^{BO}$, in evaluating total radiative cross-sections for continuum transitions. Based on a convincing but admittedly indirect numerical analysis of several previous studies we have been very confident in advancing the merits of this approximation. We have now modified our exact close-coupled codes to extract the exact half collision amplitudes without any commitment to unitarity. This new general capability of obtaining N^{+} and N^{-} directly from close-coupled codes will enjoy a wide range of applicability in continuum spectroscopy and allow us to judge the validity of the unitarity condition.

2. <u>Multichannel Semiclassical Half Collision Amplitudes</u>. In addition to solving the close-coupled equations exactly, we have developed a new simplified numerical procedure designed to obtain the half collision amplitude whenever the non-adiabatic couplings are restricted to classically accessible regions and the unitarity of N^{+} is insured. This is equivalent to solving a set of coupled semiclassical equations. We begin by choosing a set of diagonal reference potentials tailored to the nature of the exact interaction matrix. These are used to generate a set of elastically scattered WKB reference wavefunctions. Two obvious choices that we have explored in some detail are either pure diabatic, or pure adiabatic reference potentials, although in any given situation the 'preferred' choice is usually self evident. By using a random phase approximation to neglect quickly oscillating contributions to the close coupled equations we can develop a set of first order differential equations for the half collision amplitudes which are perfectly unitary, and, in appropriate and well understood circumstances, reproduce the exact close-coupled amplitudes. This multichannel semiclassical approximation is presently being applied to a number of interest situations, including multichannel curve crossings, and asymptotic frame transformation among fine-structure states.

3. <u>Multichannel Photodissociation amplitudes</u>. The expansion of our multichannel close-coupling codes to calculate photodissociation cross-sections is nearly complete. This gives very stable procedures for evaluating bound-continuum transitions, including all possible subtleties associated with non-adiabatic effects in molecular dissociation. A renormalized Numerov algorithm has been implemented into the codes for the calculation of the usual continuum-continuum S-matrix elements needed for collisional problems, but more specifically for calculation of bound-continuum transition matrix elements needed for photodissociation. This algorithm is still being tested. In particular the code is designed to calculate the final state distribution of the photofragments. Ultimately these exact matrix elements can be compared to the predictions of our half collision amplitudes based on MCQDA.

<u>Papers Completed in FY86</u>

Three papers partially supported by this research contract have been accepted or submitted for publication.

(1) "Nonadiabatic Theory of Atomic Line Broadening: Redistribution Calculations for $Sr(^1P \leftarrow ^1S)$ +Ar." P.S. Julienne and F. H. Mies, to be published in Physical Review A.

(2) "Radiative Scattering Close Coupled Calculation of Lorentzian Width and Asymmetry Parameters for Na + Rare Gas Systems" L. Vahala and P.S. Julienne, submitted to Physical Review A

(3) "Application of Recoil and Frame Transformation Models for Collisional Redistribution of Light" P.S. Julienne, L. Vahala and M.D. Havey, submitted to Physical Review A

GROWTH AND DECOMPOSITION OF GRAPHITIC STRUCTURES

Principal Investigators: S. E. Stein and R. L. Brown

Introduction

Graphitic materials are the most commonly discussed laser-armor protective materials for spacecraft. Upon laser heating, the molecular structures in these materials decompose and reform, probably in both the vapor and condensed phases. At present there exists no molecular understanding of these chemical processes. This program intends to develop this understanding in order to assist both the rational analysis of laser-induced ablation processes as well as the development of improved protective materials.

The nature and reactivity of the chemical structures formed in these processes can control the effectiveness of laser protective materials in several ways. (1) The formation rate and nature of the volatiles produced may depend on both the nature and concentrations of precursor sites in the solid as well as on the reaction mechanism. (2) The chemical structure and reactivity of the materials remaining after ablation by the initial laser pulse will be determined largely by chemical factors. (3) The condensation of carbon vapors to form refractory particles may not be controlled by diffusion, but by chemical reaction, since reformed structures must form strong chemical links to resist re-evaporation.

The development of realistic working models for the above reactions requires a substantial increase in our understanding of the structure and reactivity of graphitic species. To develop this understanding we propose to continue our combined theoretical/experimental program which focusses on the

fundamental chemical properties of very large polyaromatic structures. Graphite and nearly all carbonized organic materials are composed primarily of these structures.

Early in this program we discovered that the atomic orientation at the edges of these structures and their overall size were critically important factors in determining the reactivity of these structures. Our theoretical work has therefore been focussed on separating and examine individually these two variables. Our experimental program is devoted to examining well defined carbon deposition reactions which can be connected with our theoretical work.

Results

Theory

Our major finding during the last year has been that a modified version of classical Huckel theory is both qualitatively reliable and quantitatively accurate when applied to large polyaromatic species. In addition, we found that both the simpler theories (PMO, structure-resonance theory and other perturbation methods) and the more computationally involved SCF-methods make serious errors in their extension to very large molecules. We now have a predictive theory that we feel is not prone to major errors. Fortunately, this theory is sufficiently simple to allow calculations for molecules as large as we wish (up to several thousand carbon atoms). One important result of this application is that attack of interior carbon atoms in graphitic sheets results in a significant loss of resonance energy and is thus not likely to be an important process in graphitic systems. Another finding is that large differences in reactivity between different edge sites remains even in the limit of an arbitrarily large graphite structure. Simpler theories incorrectly predicted that all sites become equally reactive in the limit of very large cluster size. More sophisticated theories incorrectly predict a finite, edge-dependent band gap in very large clusters as well as an unreasonable bond alteration. We have also discovered that this modified Huckel method accurately predicts heats of formation of pi-radicals. This technique has not previously been thoroughly applied to these species, so that this observed accuracy strongly supports the reliability of this theoretical approach.

In general terms, edge carbon atoms behave very much like those of normal polynuclear aromatic molecules, with properties depending strongly on the local structure. Phenanthrene-like edges are rather unreactive and thermodynamically stable. They are as susceptible to free radical and electrophilic attack as are structurally related positions in naphthalene and phenanthrene. Anthracene-like edges are thermodynanamically unstable and highly reactive, with properties comparable to those of the linear polyacenes. Regardless of edge structure, interior carbon atoms situated only several bond lengths from an edge have properties (bond orders, free valence) not far from those of the interior carbon atoms in cata-condensed polyaromatic molecules like coronene. A significant general finding for the molecules studied is that there is only a weak relation between the position of the highest occupied molecular orbital and the reactivity of the most reactive position. For instance, while very large Series 3 molecules (phenanthrene-like edges, see Fig 1) will have higher HOMO energies than small Series 1 molecules (anthracene-like edges, see Fig 1), they will be far less reactive (cf., Figs. 2 and 3). This HMO method predicts that thermodynamic stability is strongly influenced by edge type. In contrast, because they utilize local properties only, group additivity methods do not predict significant edge effects.

Wave functions, which describe overall molecular properties, separate into two distinct classes for molecules with reactive edges. Those of a more stable variety are qualitatively similar to those of an infinite plane and of the molecules with stable edges. Those of a less stable variety correspond to orbitals whose electron density are located primarily at the edges. The latter variety lead to a near zero band gap, and the associated spectroscopic and electronic properties, for molecules of relatively small size. For example, a

molecule with reactive edges containing 60 carbon atoms has the same band-gap as
a molecule of the stable variety containing between 2000 and 2500 carbon atoms.

Experiment

Most of the year was devoted to the construction of a very high temperature,
low pressure flow reactor. A commercial graphite element furnace, capable of
achieving temperatures up to 3000 K has been modified and connected to a
specially-designed, differentially pumped mass spectrometric detection system.
Either molecular beam sampling or indirect detection is possible. The reactor is
made of high density graphite, with a volume of ca. 200 cm^3 and an exit aperture
of 3 mm diameter. This relatively large size will enable operation over a wide
range of well controlled pressure and chemical conditions. The inlet and flow
calibration system is near completion and will allow independent flows of two
reactants. Temperature measurement can be made by either thermocouples or
optical pyrometry.
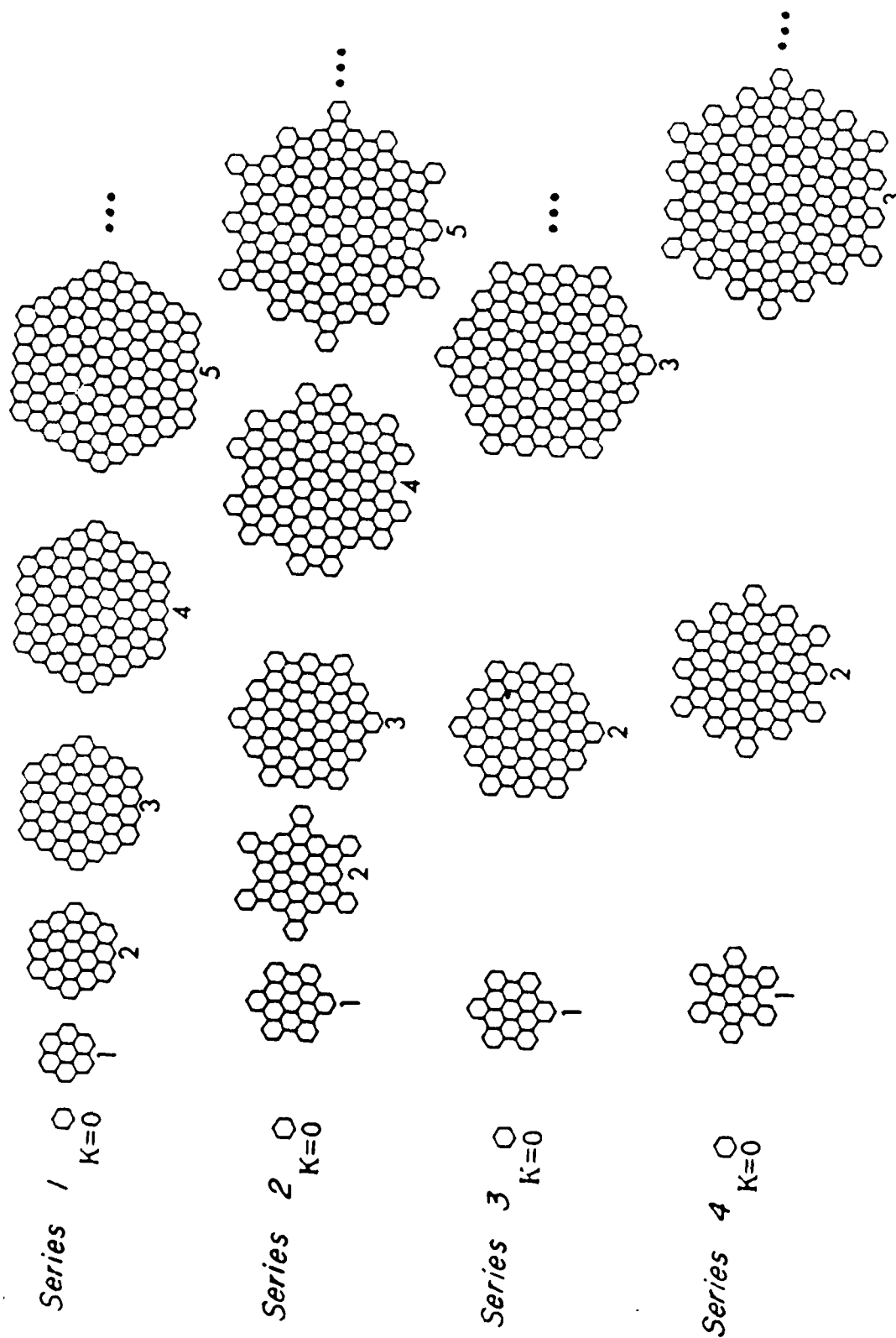
Figure Captions

Figure 1. Homologous series of hexagonally symmetric molecules.

Figure 2. Maximum free valence for each molecule in the four homologous series
as a function of molecular size.

Figure 3. Energy of highest occupied molecular orbital (HOMO) as a function of

molecular size. The reciprocal of the square root of the number N of

pi-electrons in the molecule was used for the abscissa. This was done to expand

the scale near the origin (i.e., where N goes to infinity). The value of the

Huckel electron repulsion integral is the energy unit.

Series 1
$K=0$

Series 2
$K=0$

Series 3
$K=0$

Series 4
$K=0$

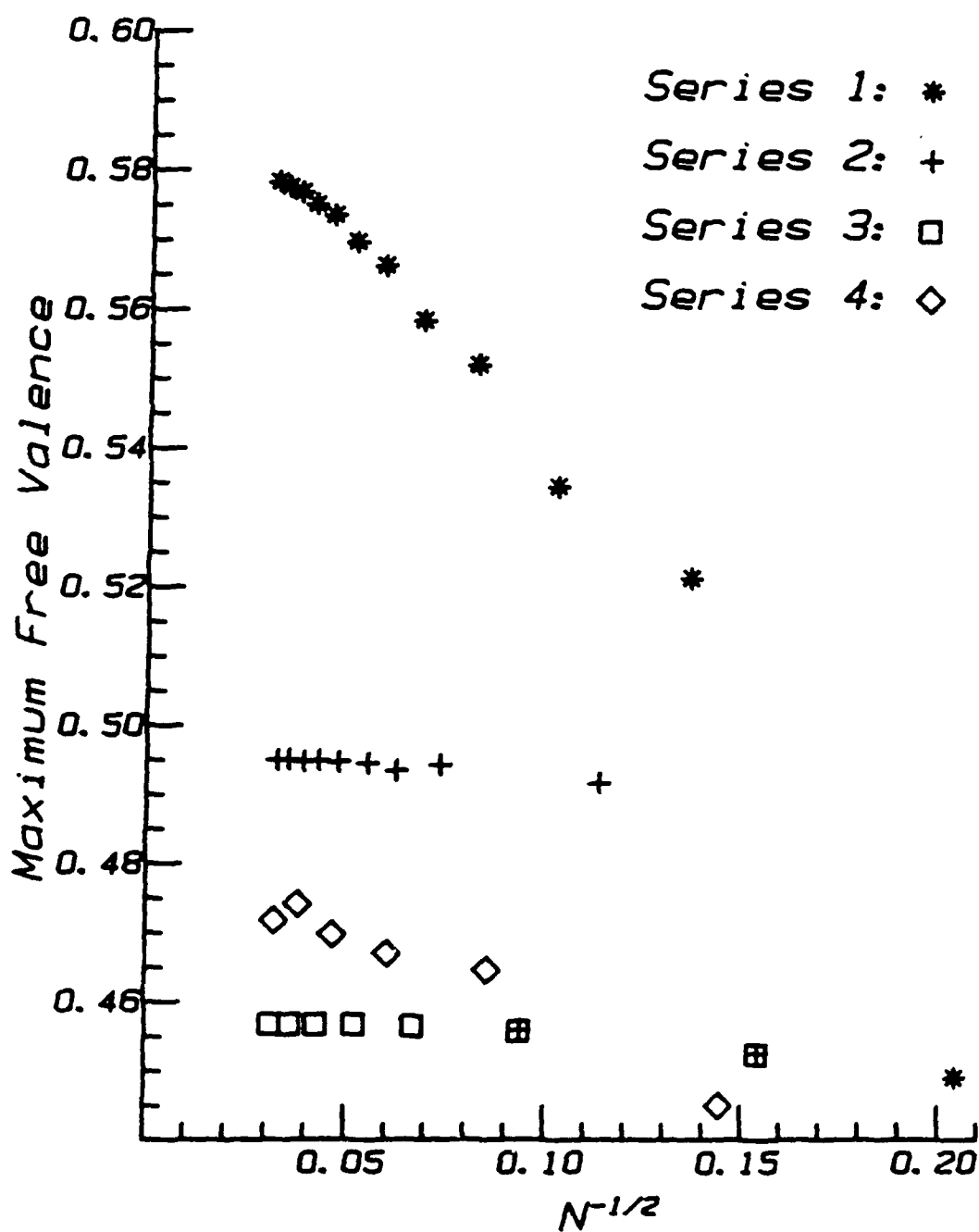Figure 1.   Homologous series of hexagonally symmetric molecules.

Figure 2. Maximum free valence for each molecule in the four homologous series as a function of molecular size.
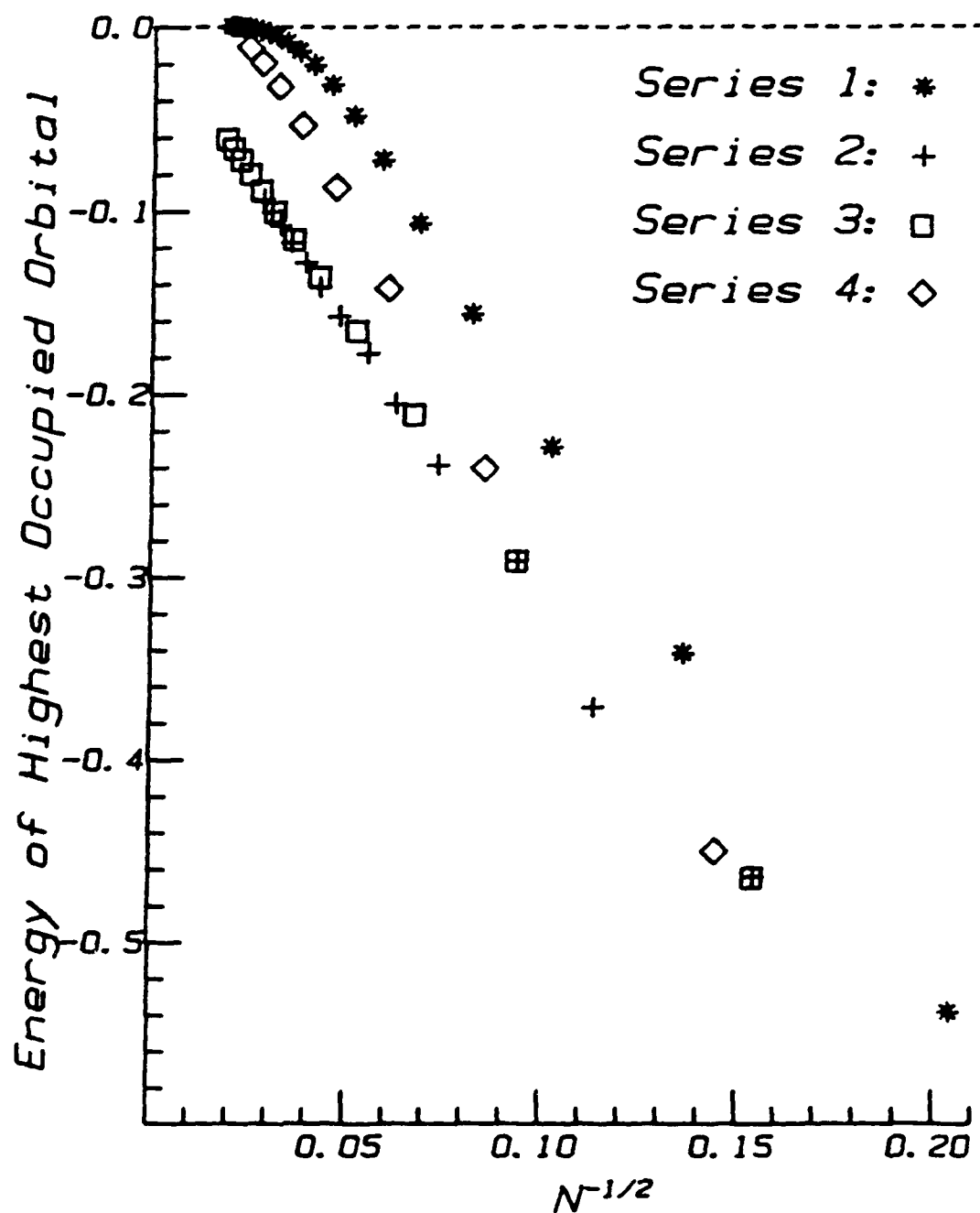
Figure 3. Energy of highest occupied molecular orbital (HOMO) as a
function of molecular size. The reciprocal of the square
root of the number N of pi-electrons in the molecule was
used for the abscissa. This was done to expand the scale
near the origin (i.e., where N goes to infinity). The
value of the Huckel electron repulsion integral is the
energy unit.

26

BUILD-UP AND IRRADIATION OF OBSCURING CLOUDS UNDER NEAR-VACUUM CONDITIONS: APPLICATION TO SPACECRAFT SURVIVABILITY

Principal Investigators: Thomas J. Buckley
                          Sharon G. Lias

For understanding the generation and dispersal of smokes and obscuring materials in space, the kinetics of evaporation of refractory materials under laser irradiation, and condensation processes leading to the formation of microscopic particles, graphitic materials and polyarylacetylenic polymers are of particular interest. This project involves the molecular-level study of ionic polymerization mechanisms in polyunsaturated linear and aromatic compounds, the structures and thermochemistry of relevant ions, the photodissociation of the polymeric ions, and the repair mechanisms which regenerated the polymeric ions after photodissociation. The model systems studied previously (diacetylene, cyanoacetylene, cyanogen, phenylacetylene and styrene)[1,2,3] were focussed on highly unsaturated organic compounds in which positive ions are generated and undergo rapid polymerization with surrounding neutral molecules (which can be identified with molecules vaporized from a graphitic surface material). The product ions from these ion/molecule reactions are larger unsaturated species which have broader absorption spectra and thus are more desirable as spacecraft obscurants.

Conclusions derived from earlier work of this project are that the highly unsaturated fragment ions (for example, $C_6H_2^+$ and $C_4H_2^+$ in phenylacetylene) react at every collision with the precursor aromatic molecules, and that efficient condensation reactions occur followed by elimination of a molecule of acetyene. The parent radical cations in these systems react with the corresponding neutral molecules to form

condensation ions, which then dissociate by the elimination of a stable molecule (benzene, hydrogen, ethylene, or acetylene for example).

The ICR cell is fitted with a quartz window, and the ions can be irradiated with (a) a xenon arc lamp fitted with various interference filters which allow one to irradiate the trapped ions with monochromatic light, and (b) an argon ion laser. Studies on the photodissociation mechanisms of parent radical cations and ionic products of ion/molecule reactions have been carried out. In these studies three different types of behavior have been seen: 1) the loss of small molecules which shorten the carbon chain, 2) the loss of a molecule of hydrogen resulting in an increase in the degree of unsaturation, 3) the loss of monomer molecules which is equivalent to depolymerization. Further, the photodissociation mechanisms of the ions have been directly determined, and the modes of reaction and structures of dissociation products have been examined. At the present time, little is known about photodissociation mechanisms of ions formed as products of ion/molecule reactions.

Work during FY86 focussed on two problem areas: (a) the chemistry of the phenylium ion ($c-C_6H_5^+$), which is ubiquitous in irradiated aromatic systems; and (b) on detailed examinations of the actual mechanisms of ionic condensation processes.

Structure and Reactivity of the Phenylium Ion

Until our recently completed work[4], little was known about the structure and reactivity of the phenylium ion. Our results have demonstrated that previous conclusions derived from collision-induced-dissociation (CID) experiments were incorrect. That is, earlier re-

sults had led to the conclusion that acyclic $C_6H_5^+$ ions are reactive with acetylene, and phenylium ions are unreactive; our study proves conclusively that the cyclic $C_6H_5^+$ are reactive, while the acyclic isomers are unreactive with aromatic molecules and alkynes. Rate constants for reactions of $C_6H_5^+$ had not previously been measured.

From ab initio calculations, it was known that the most stable $C_6H_5^+$ ion is the singlet phenylium ion, while acyclic isomers are predicted to have heats of formation at least 15 kcal/mol higher. From this knowledge of the energetics, it necessarily follows that phenylium ions are uniquely produced in the dissociative protonation of halobenzenes:

$$MH^+ + C_6H_5X \rightarrow c-C_6H_5^+ + HX + M \tag{1}$$
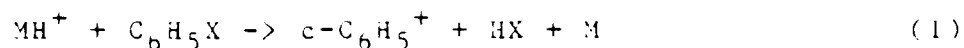
Phenylium ions must also be uniquely produced in the threshold electron-impact dissociation of the halobenzenes:

$$C_6H_5X + e \rightarrow c-C_6H_5^+ + X + 2e \tag{2}$$
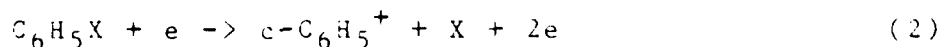
or in the low energy photodissociation of the halobenzene cations:

$$C_6H_5X^+ + hv \rightarrow c-C_6H_5^+ + X \tag{3}$$
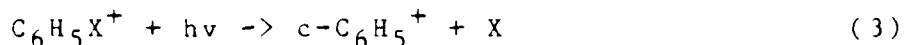
That at least two isomeric $C_6H_5^+$ ions are formed by electron impact fragmentation of organic compounds as well as in ion/molecule reactions is demonstrated by the results given in Figure 1. Figure 1, which represents the time-dependent decay of $C_6H_5^+$ ions formed in the electron-impact fragmentation of C_6H_5Cl, clearly shows that $C_6H_5^+$ populations of distinctly different reactivities exist. The reactive $C_6H_5^+$ ions exhibit a rate constant of 5×10^{-10} for the reaction:

$$C_6H_5^+ + C_6H_5Cl \rightarrow C_{12}H_{10}^+ + Cl \tag{4}$$
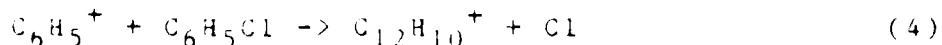
The $C_6H_5^+$ ions produced in the reaction:

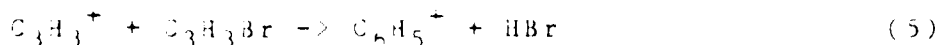$$C_3H_3^+ + C_3H_3Br \rightarrow C_6H_5^+ + HBr \tag{5}$$

exhibit the same rate constant for reaction with chlorobenzene, and therefore can be assumed to have the same structure as the reactive population of fragment ions in the aromatic system.

In order to assess which of the two populations corresponds to the phenylium ion, non-fragmenting $C_6H_5Cl^+$ ions produced with 11 eV electrons were irradiated with 2 eV photons of the argon ion laser for a short period of time, after which their decay rate was monitored. Under these conditions, only one population of $C_6H_5^+$ ions is produced; those $C_6H_5^+$ ions react with the parent chlorobenzene molecules with a reaction rate constant (5×10^{-10} cm^3/molecule-s) which is identical to that obtained for the more reactive population formed in the elect-ron impact fragmentation experiment (Figure 1). The photodissociation, which occurs through a two-photon process, can only lead to the forma-tion of phenylium ions, and therefore, it can be concluded that the reactive population has the $c-C_6H_5^+$ structure.

Because of the substantial differences in energy and energy barriers between the phenylium ion and the acyclic isomers, the iso-meric distribution of $C_6H_5^+$ species formed under any given conditions will be determined by the energy content with which the ions are formed. Thus, in acetylene, where $C_6H_5^+$ ions are generated in a simple addition reaction:

$$C_4H_3^+ + C_2H_2 \rightarrow C_6H_5^+ \qquad (6)$$

the $C_6H_5^+$ product will originate with a total energy of 353 kcal/mol; this is 82 kcal/mol above the ground state of the phenylium ion, but is not sufficient to cause dissociation. Reaction 5, which is the main secondary reaction channel in acetylene, was found to yield two $C_6H_5^+$ populations (a reactive and an unreactive), with the unreactive $C_6H_5^+$ species accounting for 60% of the total population. Although

CID experiments had led to the conclusion that the latter ions are the phenylium ions, authentic phenyl ions generated through reaction 4 reacted with acetylene in a fast reaction. The rate constant for this reaction in pure acetylene was identical to that determined for the authentic phenyl ions, thus demonstrating conclusively that the reactive, rather than the unreactive, population has the phenylium structure. The rate constant which can be ascribed to the reaction of the acyclic $C_6H_5^+$ ions with acetylene is $0.15 \pm 0.02 \times 10^{-10}$ cm^3/molecule-s, which is within experimental error the same as that obtained for the unreactive $C_6H_5^+$ ions (Figure 1) in C_6H_5Cl when C_2D_2 is added to the system.
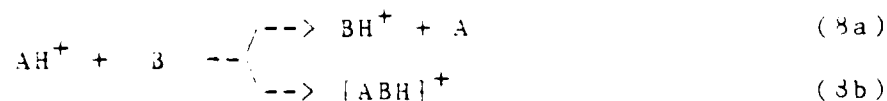
In the reaction:

$$C_3H_3^+ + C_3H_3Cl \rightarrow C_6H_5^+ + HCl \tag{7}$$
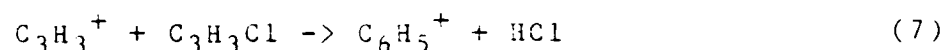
the product ions are formed with somewhat less excess energy over that of the ground state phenylium ion (<72 kcal/mol); any excess vibrational energy imparted to HCl will reduce the $C_6H_5^+$ energy content. The relatively high abundance of the unreactive population indicates that most of the energy is retained by the $C_6H_5^+$ product ion.

Ionic Condensation Mechanisms

Another study[5] explored the mechanisms of ionic condensation processes which occur without activation barriers in competition with fast proton transfer reactions:

$$AH^+ + B \quad \begin{cases} \longrightarrow BH^+ + A & (8a) \\ \longrightarrow [ABH]^+ & (8b) \end{cases}$$

The conclusions, in agreement with the results of an earlier study from this laboratory[6], were that the relative probabilities of the two

31

channels were determined by the initial configurations of the react-
ants in the collision complex, i.e. the reactions involve two
independent transition states. Evidence is also presented that when
the reactant ion has excess kinetic energy, a long-lived condensation
ion is not formed, but rather a mechanism involving a "direct" diss-
ociation occurs.

References

1. T. J. Buckley, L. W. Sieck, R. Metz, S. G. Lias, and J. F.
    Liebman, Int. J. Mass Spectrom. Ion Proc. 65, 181 (1985).

2. S. G. Lias and P. Ausloos, J. Chem. Phys. 82, 3613 (1985).

3. T. J. Buckley, and Z. Karpas, to be published.

4. P. Ausloos, S. G. Lias, and T. J. Buckley, manuscript in
    preparation.

5. Z. Karpas and S. G. Lias, J. Org. Mass Spectrom., in review.

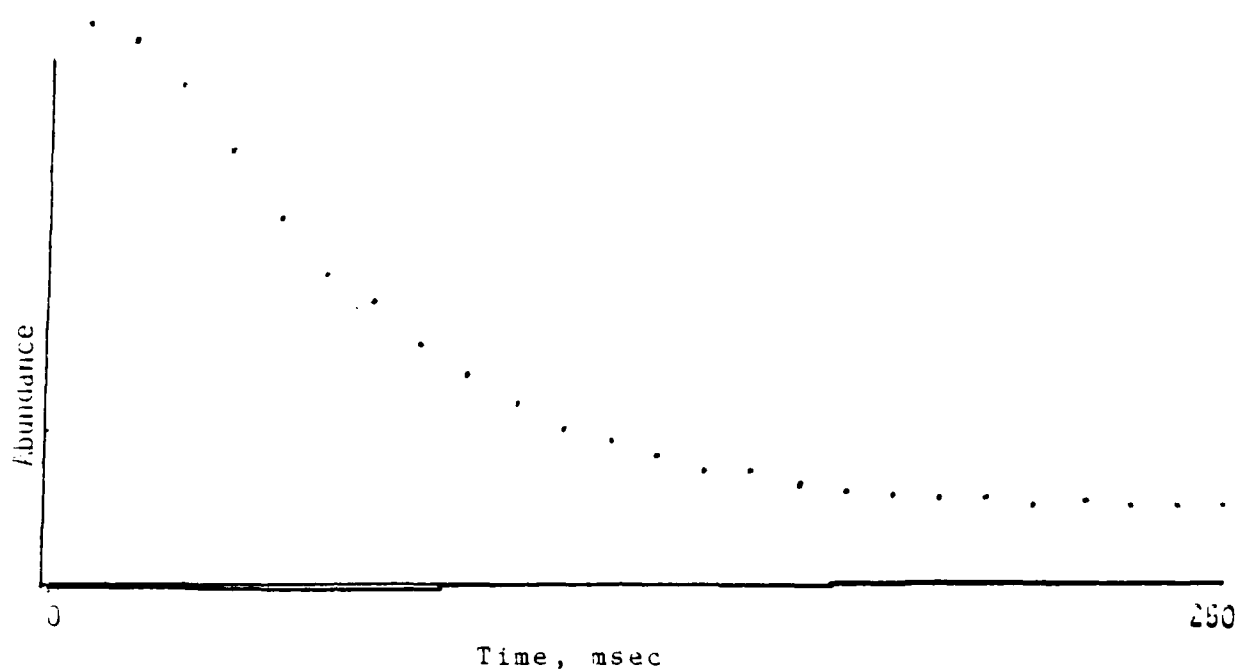6. P. Ausloos and S. G. Lias, J. Am. Chem. Soc. 108, 1792 (1986)

Figure 1.   Time dependence of the abundance of $C_6H_5^+$ formed in chlorobenzene at a total pressure of 1×10^{-6} torr, electron energy, 40 eV. From a comparison of the abundance of the unreactive population seen at long time with the total initial abundance of ions, it can be estimated that approximately 14% of the ions are in the unreactive configuration.

MOLECULAR BASIS FOR LASER-INDUCED VAPORIZATION OF REFRACTORY MATERIALS

J.W. Hastie, D.W. Bonnell, and P.K. Schenck

Ceramics Division

National Bureau of Standards

Introduction

The primary goal of this task is the development of a molecular-level understanding of the vaporization and related ionization and aggregation processes which occur when high-power laser energy interacts with refractories. Materials of current interest include graphite, and refractory carbide materials which are candidate protective materials for orbital applications. The task rationale and approach has been discussed in detail in an earlier report, NBSIR 84-2983, and recent results are described in the paper "Laser Vaporization Mass Spectrometry", submitted to Nucl. Instr. and Methods in Phys. Res. B. Beam Interactions with Materials and Atoms.

The basic experimental approach consists of coupling a high-power Nd:YAG laser with a specially designed very high pressure sampling molecular beam mass spectrometer system (VHPMS). The vacuum system provides for extremely high pumping speed, simulating near-earth orbit gas dynamics even when laser-evolved gas plumes from refractory surfaces reach pressures above one atmosphere. Using laser-synchronized detection methods, time and mass-resolved spectra of laser-induced vapor species are obtained. The mass spectrometric (MS) data provide the species specificity needed for

determination of kinetic and thermodynamic parameters of the laser heating and vaporization process when coupled with temperature and gas dynamic information.

Of particular current interest are the effects of laser energy, optical and sampling geometry, and surface morphology on the vapor species distributions (with respect to concentration and time) for a selection of graphites. Since surface temperatures in excess of 4000 K, and heating/cooling times of milliseconds, or less, are involved, new, or improved, measurement methods are required. Methods under development include techniques for determining surface and plume temperatures and the time-history of vapor species evolution.

Results for FY-86

Modification of Plume Sampling Geometry

Our previous experimental work confirmed equilibrium C_n distributions in the vapor plume for off-axis ($\geq 15°$ from surface normal) beam-sampling geometries. Also, surface temperature appeared to be independent of laser energy at surface energy loadings of 10 - 40 mJ/cm^2. The primary observed effect of increased laser power was a linear increase in species intensities but with no indication of temperature changes in the time-of-flight or species distribution data. This result suggests that a physiochemical restraint is limiting the temperature increase of the surface. Qualitative observations of deposit patterns indicated that the beam was highly forward collimated. Since the existing apparatus geometry prevented perpendicular (beam-sampling axis to plume axis angle of zero

degrees) sampling, and there was evidence of laser-plume interaction even at relatively low laser attack angles, the interaction was modified to allow sampling at angles with respect to the surface normal of between ~0° and 15°. The chamber was re-constructed with multiple access ports and an internal beam periscope but the off-axis laser impingement geometry was retained to minimize laser-vapor interactions and permit sample rastering with the in-vacuum two-axis translation stages. The new apparatus arrangement is shown in figure 1.

Initial testing indicated the need for a bench alignment procedure for adjusting the periscope, and a He-Ne laser alignment system was developed. This permits overall periscope alignment, including optimizing the external adjustments possible at the last external Nd:YAG beam steering mirror. Minor adjustments are·possible with the periscope system installed in the vacuum system to account for the significant differences between the He-Ne and Nd:YAG laser spot sizes and beam collimation.

The output coupling telescope of the Nd:YAG laser has been adjusted so that the frequency doubled Nd:YAG beam spot size is about one cm at the 30 cm focal length lens used to focus the laser on the sample. This causes the depth of focus to be smaller than with previous experiments, and allows a larger laser beam spot to impact the periscope optics, with less likelihood of laser damage to the optics in vacuum.

The final element of the periscope is a high laser power mirror, coated for 532 nm laser radiation at 45° reflection. Initial experimental work with this arrangement indicated that vapor deposition and laser damage on the mirror element was negligible. However, after extended use, it was

noted that spot damage was occuring, but with little correlation to
conditions of operation of the vacuum system. We discovered after careful
examination of the laser beam distribution that the damage was due to a
laser hot spot. It appears that the Nd:YAG beam had been developing a hot
spot for some period of time which coincidentially, and unfortunately, lead
to a best tuning pattern similar to that described by the laser operations
manual. The damage was identified as a series of small burn spots on the
laser rod. This resulted in an inability to obtain the nearly gaussian beam
pattern desirable for these studies. The rod and a damaged polarizer have
been replaced, and the laser system is again fully operational. Also, we
plan to prevent future damage by using a coated prism as the final element.

Modification of Signal Detection Apparatus

As part of the new experimental arrangement, we have implemented a
boxcar integrator-based scanning technique which permits a slow mass
spectrometer scan of an entire mass spectral region synchronous with the
laser. Figure 2 shows a block diagram of the electronics of this
experimental arrangement. The ramp generator is used via the external
command input of the quadrupole control to sweep the mass setting of the
mass spectrometer. It also provides the trigger to start the sweep of the
signal averager used to log and average the data runs. The lamp synch from
the Nd:YAG laser triggers the time base of the boxcar averager. As shown in
figure 2, the gate, or integration time, of the boxcar is positioned in
time to collect the ion signal synchronous with the laser. Since the
arrival time of the different ions are mass dependent, the width of the
gate has to be set wide enough to incoporate signals for all masses of
interest. This unfortunately increases the amount of integrated background

signal, with it's inherent noise, relative to the truly synchronous laser initiated signal. In these experiments, with the preamp input resistance set to 10^7 ohms, the gate width used is 500 us. At 20 Hz, the repetition rate of the laser, this results in a one percent duty cycle for integrating the signal. The dc. non-laser synchronous component could, in princple, be removed by simultaneous background subtraction using the second gate or channel of the boxcar averager. However, this capability was not used since it increases the inherent ac noise in the signals.

In applying a deconvolution model to the time-resolved data, we previously reported that the mass spectrometer instrumental response was a major portion of the convolution function and would need to be dramatically improved (at least by two orders of magnitude), to enable extraction of the temperature-dependent vapor-pressure generation function. In addition to pressing the state of the art in charge amplifiers, this also necessitated an improvement in time resolution. We have addressed this problem with two approaches. Initially, the mass spectrometer charge amplifier is being operated at maximum bandwidth and minimum gain (10^5 ohms). Post-amplification with a high gain differential one megahertz bandwidth oscilloscope amplifier provides the high level signals needed by the signal and boxcar averagers. We are currently investigating higher-bandwidth alternatives to the existing 100% feedback charge amplifier technology. The boxcar, introduced to permit gated detection while sweeping the mass spectrum, could also be used to gather high speed time-resolved data, but only at a very low duty cycle, i.e. one point per laser shot. To improve time resolution we have initiated a procurement for a much faster signal averager to match the higher system bandwidth. As an alternative to analog data acquisition, we have also contracted for a custom designed ultra high

38

speed multichannel scaling system, which will permit ion counting with time resolution of a microsecond or less.

Representative Results

In the new perpendicular sampling geometry, the molecular beam pattern clearly coincided with the mass spectrometer beam axis, even though the periscoped beam was directed at the surface at approximately a 15° angle. Unlike the studies at 15°, the 0° studies showed significant laser-synchronous mass spectrometer peaks at the background mass positions, and at mass peaks not identified with carbon. These data indicated that the carbon C_n (n=1-5) peaks were of similar intensity to that observed off-axis, even though estimates of macroscopic carbon transport from deposit patterns indicated more than an order of magnitude more carbon beam density on axis relative to 15° off-axis. Considerably higher than normal surface damage was also noted, which was subsequently attributed to laser hot-spotting (from the defective laser rod).

The new plume-sampling geometry and high speed signal amplification has allowed us to monitor the evolution of surface layer and impurity species from the graphite surface, using boxcar integration over regions of mass spectra, as opposed to individual mass positions. Three typical time-gated mass spectra are shown in figure 3. In figure 3a the laser is off and the mass spectrometer ionizer is on. Thus this spectrum shows the background signal integrated during the boxcar gate. The relatively high background observed here is abnormal, and was identified as a cryo pumping problem which manifested itself by an inability to adsorb permanent gases on the time scale of the laser. This problem has been resolved, and the

39

background is now negligable with respect to the plume species. The second spectrum, figure 3b, has the laser on as well as the ionizer. There is a laser-induced increase for the background signals noted in figure 3a. In addition, m/e values of 12, 23, 36 and several broad peaks above m/e of 50, appear in the spectrum. The difference between these spectra, i.e. figure 3b - figure 3a, would be the laser induced mass spectrum. The 12 and 36 m/e values are identified as C_1 and C_3, respectively. These spectra serve to illustrate the sizes of the graphite signals relative to the background. In figure 3c the laser is left on but the ionizer is turned off. In this mode of operation the signal consists only of ions formed synchronously with the laser. Comparison of the three figures indicates that the signals at values m/e of 23, 39, and 41 are mainly the result of ions formed during the laser-induced vaporization process. These peaks correspond to Na and the two K isotopes. More details about the ion detection and sensitivity are discussed below.

In the case of K at m/e 39, the m/e 41 isotope was observed with identical peak characteristics to m/e 39, and a ratio, I_{41}/I_{39} of 0.08, essentially identical to the natural abundance ratio of 0.074. The alkalies also exhibited the bimodal peak shape characteristic of other non-carbon signals, with the fast component being dominant. With the mass spectrometer electron bombardment ion source off, the fast component of Na and K was identified as transmitted ions which comprised the majority of the mass spectrometer signal. A small portion of the fast component of the carbon species is ions. It should be noted that the mass spectrometer system is intrinsically about four orders of magnitude more sensitive to ions than neutrals, as the mass spectrometer electron impact ionization process is only ~0.01% efficient. These ions apparently are part of the plume

formation process and should serve as probes of the plume. Systematic measurement of ions is planned when we have the special ion optics components and power supplies currently in procurement. In addition to the mass spectrometer studies, time-resolved optical emission (thermal) and plume fluorescence studies have been initiated.

The graphitic carbon signals of figure 4 show distinctly bimodal peaks in the ion intensity vs. time-of-arrival data, with an extremely sharp initial arrival peak which we were unable to observe with the slower signal detection electronics used previously and a superimposed slower component. The fast component of these signals appears to be the result of ions formed during the laser vaporization process and the slower component is attributed to neutrals formed during the vaporization. Ubiquitous background peaks now also appear with the very fast component and a broader component. Additional work will be required to determine how much of the very broad component of these surface species arises from electron impact fragmentation, or other effects.

Results of laser vaporization on graphite samples, which were polished to ~20-25 micron average surface roughness, were similar to those for the 100 micron surface roughness samples studied previously. With samples polished to the order of a few microns, we can begin to see individual shot damage, as expected. We experienced some sensitivity to beam focus in initiating vaporization with low angle (i.e. far from normal) laser impingement with the more highly polished samples, but are not sure how much of this difficulty resulted from the erratic beam profile behavior due to the now-replaced damaged laser rod. Scanning electron microscope work to examine the microstructure of the impact zones is in progress.

41

FIGURE CAPTIONS

Figure 1. New Experimental Arrangement, showing beam periscope and in-vacuum x-y translator (dimensions not to scale).

Figure 2. Block Diagram of Electronics for Scanned Gated Detection of Mass Spectra.

Figure 3. Scanned Gated Mass Spectra of Graphite.

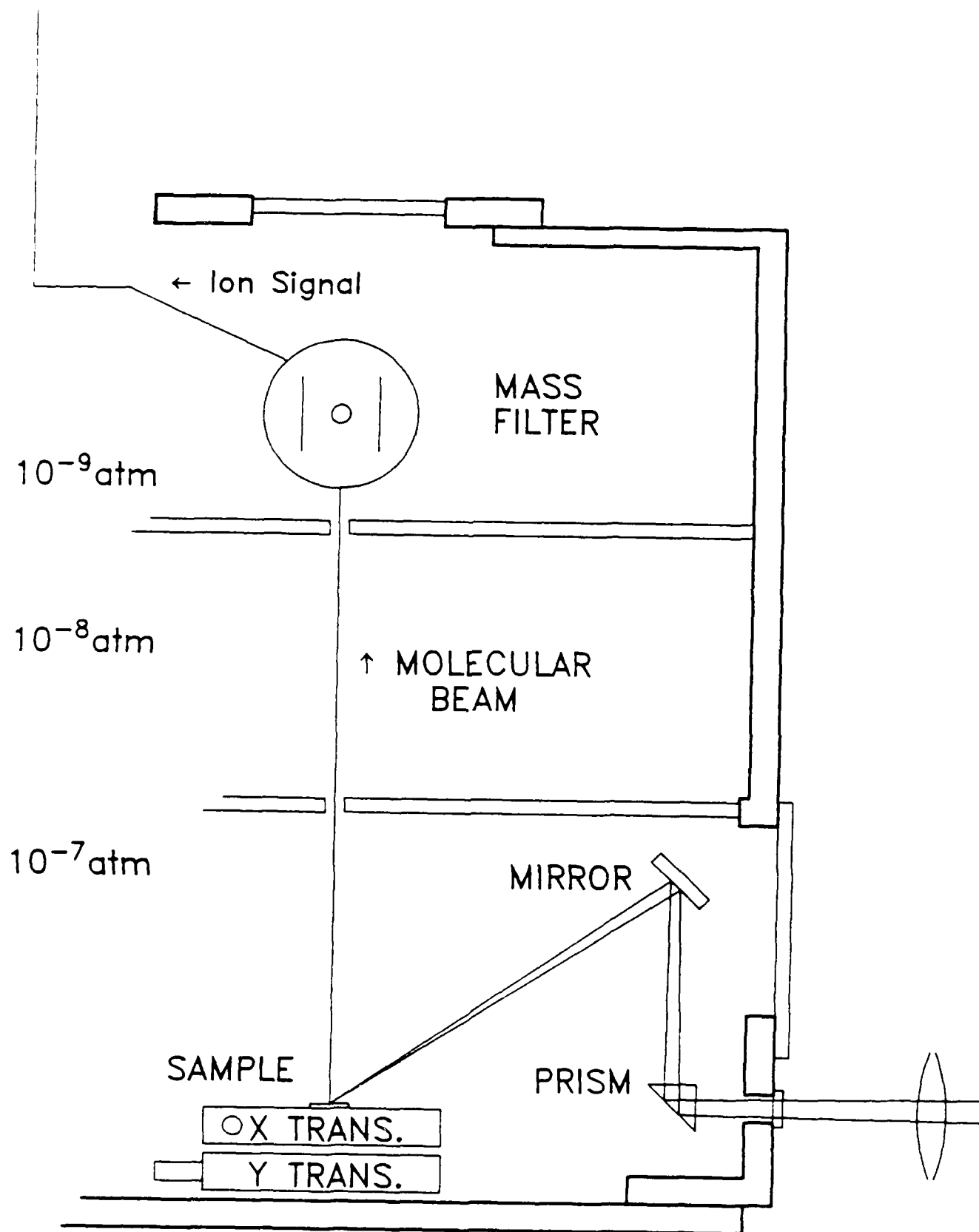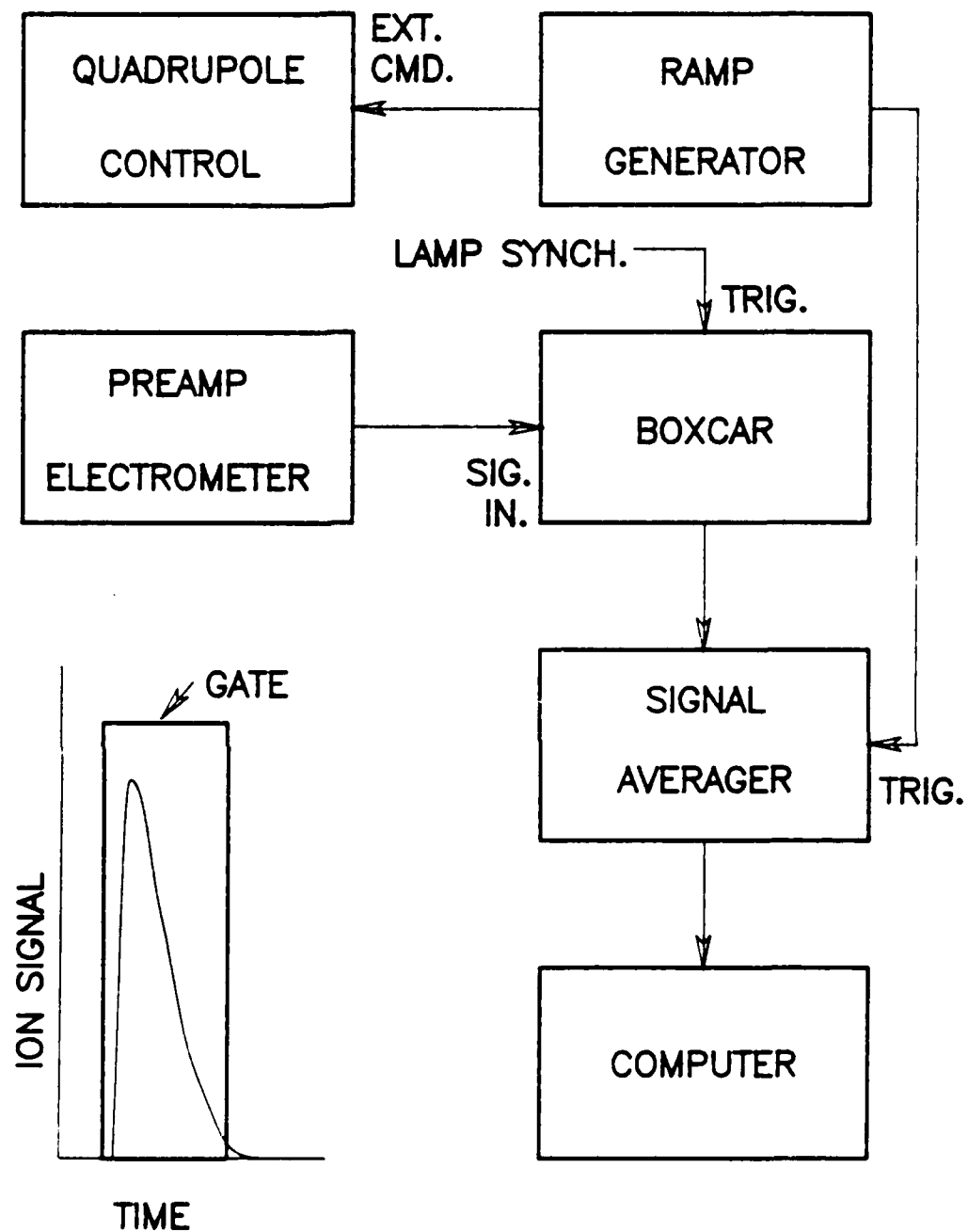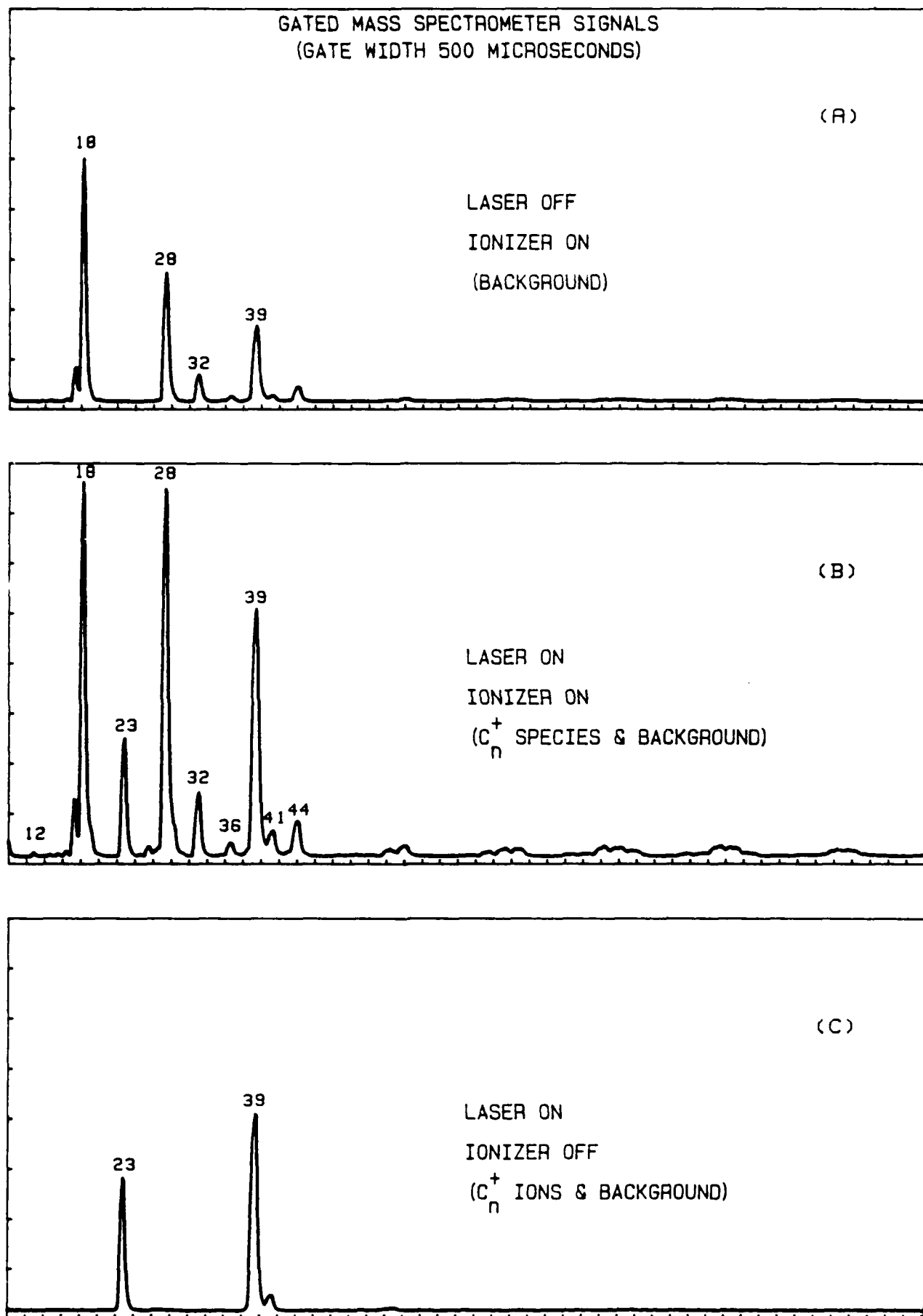Figure 4. Time-Resolved Mass Spectrometer Signals.

Figure

Figure 2

GATED MASS SPECTROMETER SIGNALS
(GATE WIDTH 500 MICROSECONDS)

(A)

18
28
32
39

LASER OFF

IONIZER ON

(BACKGROUND)

(B)

18
28
39
23
32
12
36
41
44

LASER ON

IONIZER ON

(C_n^+ SPECIES & BACKGROUND)

(C)

39
23

LASER ON

IONIZER OFF

(C_n^+ IONS & BACKGROUND)

Figure 3

END

4-87

DTIC